The Astrophysical Journal, 715:59–65, 2010 May 20 doi:10.1088/0004-637X/715/1/59
© 2010. The American Astronomical Society. All rights reserved. Printed in the U.S.A.

CONSTRAINING THREE-DIMENSIONAL MAGNETIC FIELD EXTRAPOLATIONS USING THE TWIN PERSPECTIVES OF *STEREO*

Paul A. Conlon and Peter T. Gallagher
Astrophysics Research Group, School of Physics, Trinity College Dublin, Dublin 2, Republic of Ireland
Received 2009 September 25; accepted 2010 April 1; published 2010 April 23

ABSTRACT

The three-dimensional magnetic topology of a solar active region (NOAA 10956) was reconstructed using a linear force-free field extrapolation constrained using the twin perspectives of *STEREO*. A set of coronal field configurations was initially generated from extrapolations of the photospheric magnetic field observed by the Michelson Doppler Imager on *SOHO*. Using an EUV intensity-based cost function, the extrapolated field lines that were most consistent with 171 Å passband images from the Extreme UltraViolet Imager on *STEREO* were identified. This facilitated quantitative constraints to be placed on the twist (α) of the extrapolated field lines, where $\nabla \times \mathbf{B} = \alpha\mathbf{B}$. Using the constrained values of α, the evolution in time of twist, connectivity, and magnetic energy were then studied. A flux emergence event was found to result in significant changes in the magnetic topology and total magnetic energy of the region.

Key words: Sun: corona – Sun: flares – magnetic fields

1. INTRODUCTION

Extreme solar events such as solar flares and coronal mass ejections (CMEs) originate in the corona of active regions. As the corona is a low-β plasma, the magnetic field rather than the gas pressure governs its structure and evolution (Gary 2001). This enables force-free field extrapolations of the photospheric field to be used to study the detailed topology of the solar corona (Longcope et al. 2009). Of particular interest to space weather applications is how the three-dimensional (3D) field topology of active regions governs the production of extreme solar events. Unfortunately, previous attempts to reconstruct the 3D topology of active region fields have been limited by observational issues, such as incomplete measurements of the photospheric vector field, or theoretical issues such as ill-constrained extrapolation algorithms (e.g., DeRosa et al. 2009, and references within). With the launch in 2006 December of the *Solar TErrestrial RElations Observatory* (*STEREO*) satellites, the observational limitations on reconstructing the 3D topology of active regions have largely been overcome, thus opening a new era in the study of the ever-changing solar corona.

Observations of the coronal magnetic field are difficult to obtain due to the tenuous nature of the corona and the absence of strong magnetically sensitive emission lines. Estimates of the strength of the coronal magnetic field are possible using radio observations, however, this remains a difficult problem requiring simultaneous knowledge of both the temperature and density of the solar atmosphere (Brosius & White 2006). In order to overcome these issues, modelers have developed a variety of theoretical techniques to examine the topology of the coronal magnetic field (Gary 1989; Mikic et al. 1990). These methods require observations of the photospheric or chromospheric magnetic field as boundary conditions for the extrapolations. Well-constrained extrapolations are normally produced using photospheric vector magnetograms, although Metcalf et al. (1995, 2002) have developed methods that make use of chromospheric vector magnetograms. As the chromosphere is in a force-free state, chromospheric vector magnetograms are ideally suited as boundary conditions in force-free extrapolation methods. However, these observations have a limited field of view and spatial and temporal resolution. As such, photospheric magnetograms are commonly used as boundary conditions for magnetic field extrapolations.

The extrapolation of the photospheric field into the corona requires that a number of assumptions be made. First, it is assumed that the coronal magnetic field remains stable for the duration of the observation. Therefore, a static magnetic field model is normally used. In addition, it is reasonable to assume that the field is in a force-free configuration. This results in a vanishing Lorentz force, $\mathbf{j} \times \mathbf{B} = 0$, where $\mathbf{j}$ is the current density, $\mathbf{B}$ is the magnetic field. The force-free condition requires that the current density remains parallel to the magnetic field, $\mu_0\mathbf{j} = \alpha\mathbf{B}$, and therefore $\nabla \times \mathbf{B} = \alpha\mathbf{B}$, where α is the amount of twist in the field and is some times referred to as the torsion function. In the case of $\alpha = \alpha(\mathbf{r})$, the governing equations become $\nabla \times \mathbf{B} = \alpha(\mathbf{r})\mathbf{B}$ and $\mathbf{B} \cdot \nabla\alpha(\mathbf{r}) = 0$. This nonlinear force-free (NLFF) field is the generic solution to the force-free field condition. Complete knowledge of the photospheric magnetic field allows for the inversion of the preceding equations and the calculation of α at each point on the photosphere. As such, vector magnetograms are required to calculate the NLFF field in the corona (Schrijver et al. 2006). While NLFF methods offer the possibility of increased accuracy, they are computationally intensive. Additionally, NLFF extrapolation suffers from several other sources of error, such as the limited field of view, non-force-free nature of the photospheric field, the intrinsic 180°ambiguity, and low signal to noise of the transverse component of vector magnetograms (DeRosa et al. 2009). Forcing $\alpha = 0$ results in the potential or current-free solution, which is a first-order approximation to the coronal magnetic topology. The potential field solution is the first of two subclasses of solutions to the force-free field. Given the reduced complexity of the potential solution, the only boundary conditions necessary to form a solvable set of equation are measurements of the line-of-sight (LOS) magnetic field (Gary 1989). The second and final subclass of solution to the force-free field is the linear force-free (LFF) field, where $\alpha =$ constant and $\nabla \times \mathbf{B} = \alpha\mathbf{B}$. Assuming that α is constant for all field lines allows for the formation of a closed set of equations with only knowledge of the LOS magnetic field, provided α is predefined (Alissandrakis 1981).

A major difficulty in studying the extrapolated field line distribution is deciding on what is the most appropriate way to constrain α. Leka & Skumanich (1999) and more recently Burnette et al. (2004) compared three methods and applied them to a single active region. The first method considered was based on the best-fit value of α from an LFF extrapolation of a longitudinal magnetogram that best matched the horizontal field of the corresponding vector magnetogram (Pevtsov et al. 1995). Second, the value of α was chosen from the mean of the distribution of local $\alpha_z = \alpha(x, y)$ (Pevtsov et al. 1994). In the final method, the value of $\alpha = J_z/B_z$ was inferred from the slope of a least-squares linear fit to the distribution of local $J_z(x, y)$ versus $B_z(x, y)$. Burnette et al. (2004) conducted a detailed study of these three methods, concluding that they give statistically consistent values of α. As the methods described above require the availability of high quality vector magnetograms, they are not always an available option for constraining the values of α.

EUV and X-ray images of emitting coronal structures, mainly loops, can also be used to constrain the choice of α in magnetic field extrapolations. Initially, loop tracing methods were used to provide a first guess at the structure of coronal loops and through the application of numerical methods the 3D structure found (Aschwanden et al. 1999). Other authors have developed methods that minimize the separation between the field lines calculated from observations and extrapolations as a constraint on the choice of α (Lim et al. 2007). Wiegelmann et al. (2005), Carcedo et al. (2003), and Aschwanden et al. (2008a) developed related techniques that examine the EUV emission of coronal loop structures and retrieve their two-dimensional structure using a cost function method. Wiegelmann et al. (2005) developed a cost function grading method to evaluate the agreement of calculated field lines and the observed emission of coronal loops. This enabled them to gauge the optimum value of α for a small number of LFF extrapolations. The cost function method was found to allow for the selection of the optimum value of α used in the LFF extrapolations, however, the number of possible values of α examined was insufficient to allow for a detailed study of the active region. Most recently, Aschwanden et al. (2008b, 2009) expanded on the methods discussed above with the use of the *STEREO* spacecraft to study the structure and oscillations of coronal loops.

Once the value of the magnetic twist (α) in a region has been well constrained, an accurate estimate of the magnetic energy or more importantly, the free magnetic energy, can be estimated. The magnetic energy budget of active regions can be calculated using volume-integral and surface-integral methods such as the magnetic virial theorem (Emslie et al. 2004). The free energy is calculated as the difference between the magnetic energy of the NLFF field and that of a lower bound such as the potential (current-free) field. These methods have shown the free energy in active region's to be in the range of 10^{32}–10^{33} erg depending on the size of the region (Gary 1989; Régnier & Priest 2007; Metcalf et al. 1995, 2005). The magnetic virial theorem assumes that the measured field is a force-free field and is only possible if the measured data are force-free consistent. Additionally, knowing the topology of the active region at instances during its evolution, changes in the regions connectivity can be examined. Studies of the changing connectivity of active regions using a combination of active region segmentation techniques and magnetic field extrapolations have been achieved (Longcope 2001; Longcope & Beveridge 2007; Longcope et al. 2009). Longcope et al. (2009) concluded that comparison of the changing connectivity in active region over time could provide insight into energetics and reconnection in the coronal fields.

The methods described in this paper allow for the 3D structure of the magnetic field of an active region to be recovered and a detailed analysis of its evolution to be performed using *Solar and Heliospheric Observatory* (*SOHO*) Michelson Doppler Imager (MDI; Scherrer et al. 1995) LOS magnetograms and *STEREO* Extreme UltraViolet Imager (EUVI; Howard et al. 2000) images. The observation and the transformation of coordinates between *STEREO* and *SOHO* reference frames are outlined in Section 2, while details of the extrapolation method and the cost function are then given in Section 3. Our results, relating to twist, connectivity, and magnetic energy are presented in Section 4, and our conclusions are given in Section 5.

2. OBSERVATIONS

NOAA 10956 produced a *GOES* class B9 flare on 2007 May 19. Associated with this flare was a CME and a globally propagating disturbance within the solar corona (Long et al. 2008). Extrapolations of the region's coronal magnetic field were constrained at the lower boundary with LOS magnetic field measurements obtained by MDI on *SOHO*. MDI images the Sun on a 1024×1024 pixel^2 CCD camera through a series of increasingly narrow filters (Scherrer et al. 1995). A pair of tunable Michelson interferometers enable MDI to record filtergrams with an FWHM bandwidth of 94 mÅ. In this work 96-minute cadence magnetograms of the solar disk with a pixel size of $\sim 2''$ are used.

Images from EUVI, part of the Solar Earth Connection Coronal and Heliospheric Investigation (SECCHI; Howard et al. 2000) suite of instruments on board both *STEREO* (*A*)*head* and (*B*)*ehind*, were used in order to constrain the choice of α within the LFF extrapolation of the corona. In particular, 171 Å images from EUVI were used as this passband has fewer contributions from diffuse higher temperature emission lines compared to 195 Å images (Phillips et al. 2005). These results in more defined loops which are easier to compare by the methods described in Section 3. Each *STEREO* image was co-aligned with a common *SOHO* MDI image using a transformation method based on the work of Aschwanden et al. (2008b), so as to allow the transformation of points between the *STEREO A*, *B*, and *SOHO* reference frames.

3. METHODS

Given the limited reliability of vector magnetograms and the errors associated with their use in NLFF methods, an LFF method is used in this study to recover the coronal field as accurately as possible. Assuming a force-free field, $\mathbf{j} \times \mathbf{B} = \mathbf{0}$, an LFF field is governed by

$$\nabla \times \mathbf{B} = \alpha \mathbf{B}, \tag{1}$$

where α = constant. For LFF field extrapolations, α is a predefined free parameter. Small changes in α result in large changes to the extrapolated field. Comparing extrapolated field lines with EUV observations provides a method of restricting α and improving the accuracy of our results.

It is possible to systematically determine the value of α that provides the best possible comparison with the EUV observations using the following steps.

1. Compute the LFF field.
2. Calculate a large number of possible magnetic field lines.

3. Project field lines onto EUV observation.
4. Calculate the cost function along each field line.
5. Repeat for each additional value of α.
6. Compare the cost of the best matched field lines for each α.

In order to do this accurately, it was first important to define what a *good field line* is. Figure 1 shows the path and resulting intensity for three different ideal field lines. Field line "A" crosses the bright emission only once and has a small spike in emission along its length. Field line "B" rests along the field line and has a smooth bright intensity profile. Field line "C" oscillates on and off the bright emission and the resulting profile has a series of spikes in the intensity. With this in mind, a number of methods have been developed to systematically extract loop profiles from EUV image of the solar corona (Carcedo et al. 2003; Wiegelmann et al. 2005). Including this information in the definition of a cost function used to constrain the choice of α removes the intermediate step of extracting coronal loop profiles. For the purposes of this research, modifications to the Wiegelmann et al. (2005) method were studied to find the most computationally efficient and best performing cost function. A small sample of the various cost functions studied are

$$C_W = \int \nabla I(l)dl \Big/ \left(l \left(\int I(l)dl \right)^2 \right),$$

$$C_{\mathrm{EW}} = \int \nabla I(l)dl \Big/ \left(l \int I(l)dl \right),$$

$$C_B = 1 \Big/ \int I(l)dl,$$

where $I(l)$ is the intensity of emission along a loop and l is the loop length, C_W and C_{EW} are the standard and equal weight cost functions as defined by Wiegelmann et al. (2005), and C_B is a modified cost function developed to select the brightest field lines.

Using the LFF method from Alissandrakis (1981), field lines were extrapolated starting from a user-defined footpoint. Footpoints were selected from EUV observations of the coronal loops in question. Field lines were then transformed to the desired perspective of each *STEREO* spacecraft, and the emission along each field line and associated cost calculated. Figure 2 (top) shows the ability of the three cost functions to recover the geometry of the active region loop. As can be seen, the C_{EW} and C_W cost functions perform best, both however include unrealistic field lines. These are due to the infinite number of possible field line paths leaving any sub-region of the active region. Given the tenuous nature of the coronal loops we wish to study, field lines that cross the core of the region and other high emission locations will have unacceptable paths and relatively low costs.

In order to overcome this, field lines were forced to emerge from user-defined footpoints and pass through a number of guide circles. These user-defined guide circle domains are highlighted in Figure 2 (bottom). Figure 2 (bottom) shows the ability of the three cost functions to recover the geometry of the active region loop with the inclusion of these guiding circles. This can be seen to greatly increase the ability of each cost functions to recover the coronal geometry. The C_{EW} cost function was used in this work to select the value of α for the LFF extrapolations due to its ability to select more valid field lines under both conditions. The user-defined footpoints and guide circles stop the algorithm from selecting loops and other bright features outside the region of interest. Large guide circles, with radii less than a typical

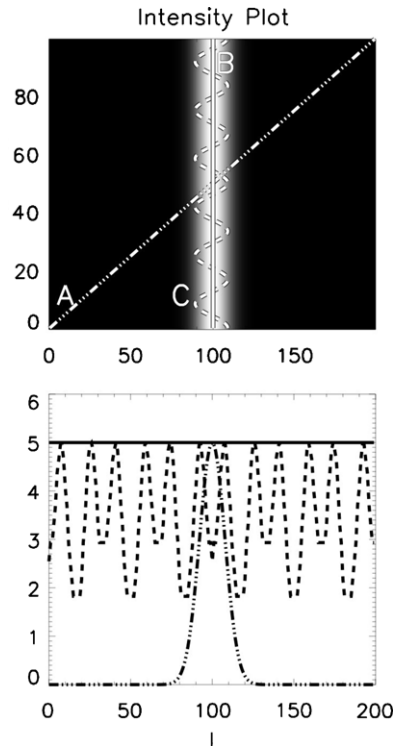

Figure 1. Field lines overlaid on emission with a Gaussian profile. Top: bright Gaussian ridge, with three overlaid field lines "A," "B," and "C." Field line "A" crosses the ridge, "B" rests along the ridge, and "C" oscillates along the ridge. Bottom: intensity as measured along each field line.

loop half-length, were chosen to ensure that any difference in user selections would result in similar features being used to constrain the extrapolations. It may, in the future, be possible to automate the selection of coronal loops based on EUV and/or X-ray emission, but this will require the application of an accurate and robust coronal loop detection algorithm (e.g., Aschwanden et al., 2008a).

Using the C_{EW} cost function, it is possible to compare the cost function for various values of α and determine the value that most closely resembles the observed field. More than 5000 field lines are plotted for each value of α and the cost along each is calculated. In order to enhance the sensitivity of the method to changes in the values of α only, the total cost of the 15 best field lines is compared. As shown in Figure 2, this is a sufficient number of field lines to accurately recover the topology of the region. The contrast of the cost for each value of α was increased further by normalizing the returned values and setting the cost to 1 for values of α where no field lines pass through the guiding path and/or end at the user-defined footpoint.

Figure 3 shows the best field lines as selected by the method for *STEREO* EUVI images from both the *A* and *B* spacecraft. The field lines returned by the method are not the same for each spacecraft. However, the general geometry defined by the field lines is very similar. Figure 4 shows the field lines from both perspectives plotted together in 3D.

An estimate of the energy of the LFF field in excess of the potential field can be obtained from

$$E_{\mathrm{Diff}} = E_{\mathrm{LFF}} - E_{\mathrm{Pot}}, \tag{2}$$

where E_{LFF} is the magnetic energy of the LFF field

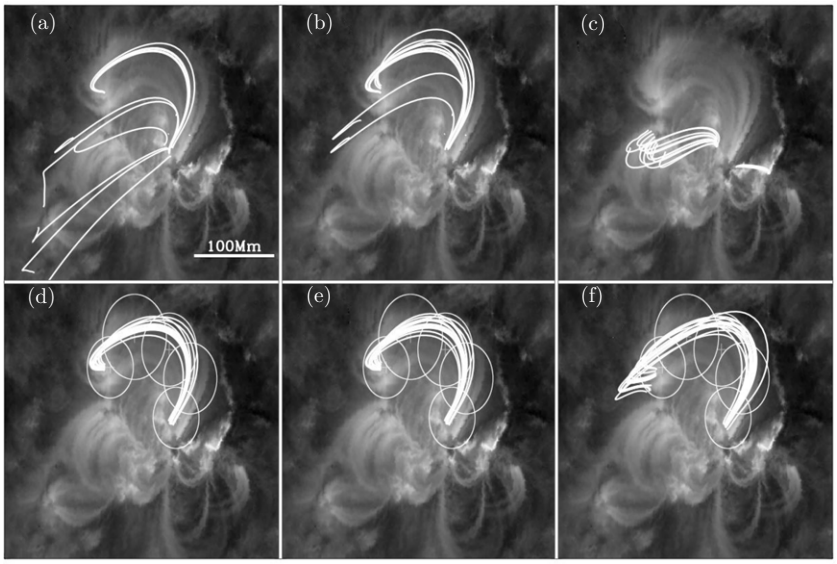

Figure 2. Field lines that best represent the observed emission as calculated by the selection algorithm for $\alpha = 6.25 \times 10^{-3}$ Mm^{-1}. (a) C_W, (b) $C_{\rm EW}$, and (c) C_B cost functions without field line path restrictions. (d), (e), and (f) Same with field line path restriction as outlined with overlaid circles.

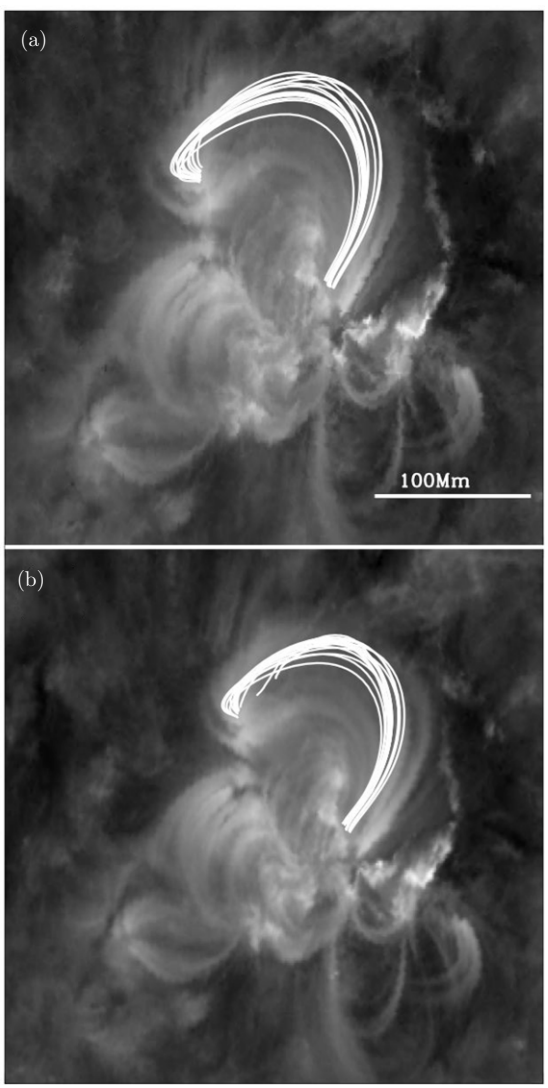

Figure 3. Top: 15 field lines with the smallest cost as selected using the $C_{\rm EW}$ cost function with *STEREO A* EUVI images of NOAA 10956. Bottom: the same but for *STEREO B* images, for $\alpha = 8.7 \times 10^{-3}$ Mm^{-1}.

extrapolation,

$$E_{\rm LFF} = \int \left(\mathbf{B}_{\rm LFF}^2/8\pi\right) dV, \tag{3}$$

and $E_{\rm pot}$ is the energy of the potential field extrapolation,

$$E_{\rm Pot} = \int \left(\mathbf{B}_{\rm Pot}^2/8\pi\right) dV, \tag{4}$$

where dV is a volume within the computational domain, and $E_{\rm Pot}$ and $E_{\rm LFF}$ are the magnetic energy of the potential field and LFF field, respectively.

As a precautionary warning, it should be noted that LFF extrapolations have a maximum value of α that can be studied before oscillatory signals from the complex solution of the governing set of equation begin to dominate the systems (Gary 1989). We have investigated this effect for the data set studied here and found that for α values up to 0.03 Mm^{-1} the oscillatory signal from the complex solutions is negligible up to a height of 100 Mm, the maximum height of loops studied here.

4. RESULTS

Using the method described in Section 3, an initial investigation of the cost function behavior for a range of α values from -0.3 Mm^{-1} to 0.3 Mm^{-1} had established that a minimum in the cost function existed and had a positive value of α. To verify this, a more detailed analysis of the cost function was conducted for 23 values of α within the range of -0.11 Mm^{-1} to 0.28 Mm^{-1}. Figure 5 shows the evolution of the cost function for these values of α at the times studied. At all times, there is a strong correlation between both the *STEREO A* and *B* cost functions. At 09:35 UT, there is a distinct minimum in the cost at 5×10^{-3} Mm^{-1}. The cost for the *STEREO B* observations was seen to decrease for larger values of α, however, as the *STEREO A* cost does not follow this trend it is assumed false. At 11:11 UT, the minimum has increased to around 1×10^{-2} Mm^{-1}, the relatively high cost returned for $\alpha = 5 \times 10^{-3}$ Mm^{-1} reinforces this increase. From 12:47 UT onward, the minimum cost in α or twist of the coronal loop analyzed is seen to decrease to levels seen at 09:35 UT.

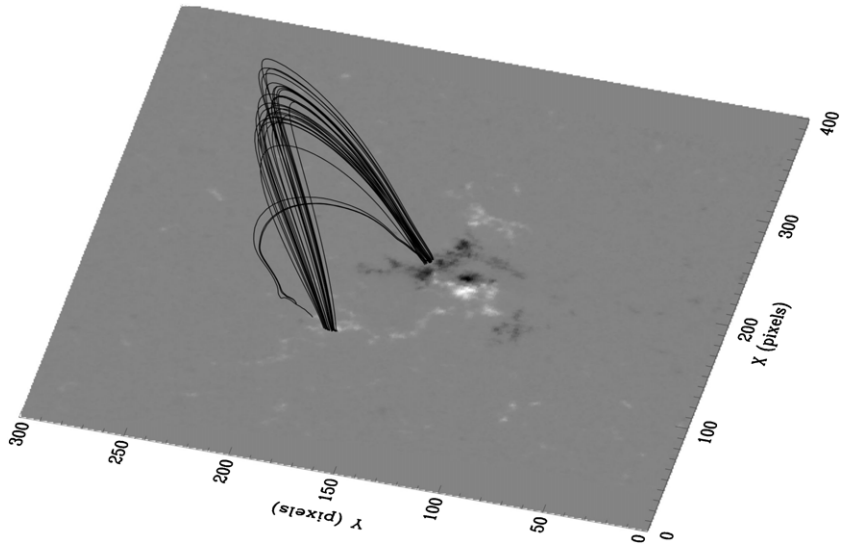

Figure 4. 3D view of field lines as shown in Figure 3.

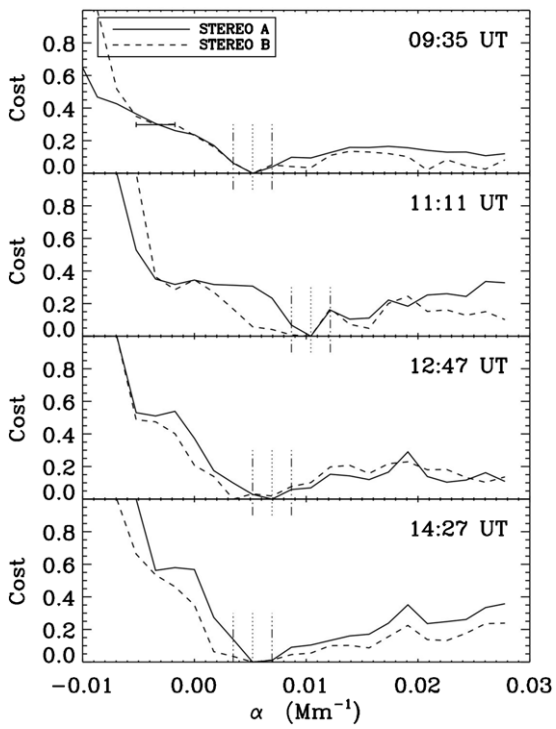

Figure 5. Top to bottom: cost for a range of α values for MDI magnetograms obtained at 09:35 UT, 11:11 UT, 12:47 UT, and 14:27 UT. Solid and dashed lines represent comparisons with *STEREO A* and *B* EUVI observations, respectively. Error bars in top panel represent the associate error in all the values of α due to the step size used in the calculations. Minimum in the cost function and the associated error are highlighted by the vertical dotted lines and dash-dotted lines, respectively. The active region produced a B9 flare that began at ∼12:34 UT, peaked at ∼13:02 UT, and ended at ∼13:19 UT.

The evolution of magnetic flux within each sub-region was examined in order to more fully understand these changes in α. Each magnetogram image of NOAA 10956 was thresholded at the ±100 G level to identify the main regions of magnetic flux in the global structure. Figure 6 shows the main positive and negative sub-regions within the active region, ranked by area from largest to smallest. From the corresponding *STEREO*/EUVI image, it is clear that the large loop structure studied here is associated with field lines connecting regions 1^- and 3^+. Table 1 summarizes the changing magnetic flux within the region (some negative regions are excluded due to changes in ranking during the time studied).

Table 1
Evolution of the Magnetic Flux in the Major Sub-regions Contained Within NOAA 10956

Region	09:35 UT	11:11 UT	12:47 UT	14:27 UT
1^-	77.8	76.5	76.5	76.9
1^+	32.5	33.1	33.7	34.5
2^+	12.5	11.4	11.7	11.9
3^+	7.2	7.1	6.8	8.6
4^+	3.3	3.4	3.7	2.1

Note. Results are reported in 10^{20} Mx.

As can be seen there was a significant changes in the magnetic flux in the region during the time analyzed. From 09:35 UT to 11:11 UT, the magnetic flux in region 1^+ increased by 0.6×10^{20} Mx, while in regions 1^- and 2^+ the magnetic flux decreased by 1.3×10^{20} Mx and 1.1×10^{20} Mx, respectively. During this time, the other sub-regions saw little or no changes in their magnetic flux. From 11:11 UT to 12:47 UT, the magnetic flux in regions 1^+ and 2^+ increased by 0.6×10^{20} Mx and 0.3×10^{20} Mx, respectively. While the magnetic flux in region 3^+ decreased by 0.3×10^{20} Mx. From 12:47 UT to 14:27 UT, the magnetic flux in regions 1^+, 1^-, and 3^+ increased by 0.8×10^{20} Mx, 0.4×10^{20} Mx, and 1.8×10^{20} Mx, respectively.

Knowing the values of α, it is then possible to study changes in the connectivity within the region. As region 1^- is the common footpoint for most of the loops in the active region, it was selected as the source for all the extrapolated field lines used to examine the region's changing connectivity. Table 2 outlines the changing connectivity for the time studied. From 09:35 UT to 11:11 UT, the major changes in connectivity are associated with the transfer of flux from a closed to open configuration and a 1.9% increase in flux connecting region 1^- to region 4^+. From 11:11 UT to 12:47 UT, there is a decrease in the amount of open flux and an increase in the connectivity from region 1^- to regions 1^+, 2^+, and 3^+ by 4.8%, 0.8%, and 2.3%, respectively. Additionally, the amount of flux joining region 1^- to region 4^+ decreases by 3%. From 12:47 UT to 14:27 UT, the amount

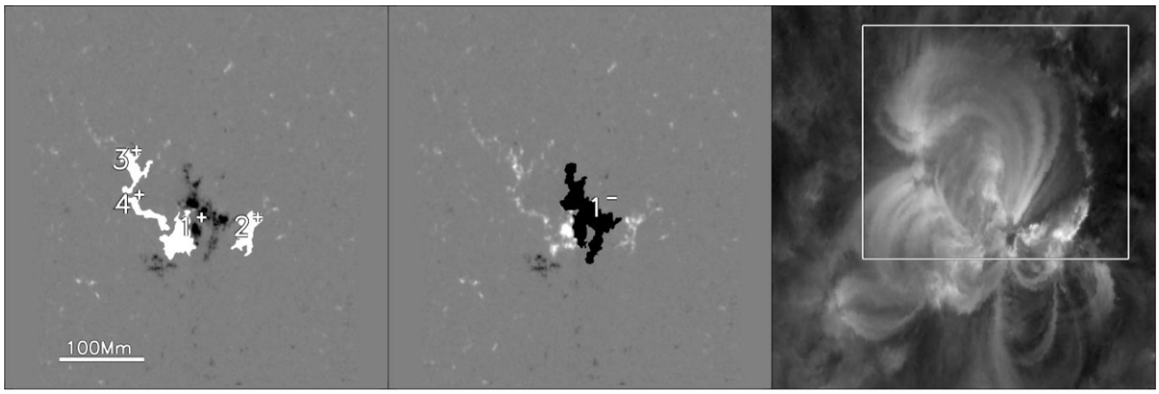

Figure 6. Sub-regions of NOAA 10956. Left panel: positive regions identified by thresholding, ranked in order of area. Middle panel: the same for negative regions. Right panel: corresponding *STEREO*/EUVI image. The smaller volume centered on the observed loop used for the energy calculations is illustrated by the box shown.

Table 2
Connectivity Matrix for Field Lines Starting at Region 1^-, with Threshold of ±50 G

1^-	09:35 UT	11:11 UT	12:47 UT	14:27 UT
Open	13.9	20.6	15.9	12.9
Closed	31.9	24.3	23.8	23.6
1^+	24.5	25.1	29.8	38.9
2^+	11.1	10.8	11.6	11.2
3^+	9.8	9.7	12.0	12.3
4^+	7.4	9.3	6.2	0.00

Note. All results are a percentage of total flux leaving region 1^-.

Table 3
Changes in the Magnetic Energy Contained within Different Volumes in NOAA 10956

Size	Parameter	09:35 UT	11:11 UT	12:47 UT	14:27 UT
Small region	Pot	4.46	4.44	4.44	4.48
	LFF	4.48	4.50	4.46	4.49
	Difference	0.013	0.061	0.021	0.01
Full volume	Pot	6.51	6.38	6.33	6.23
	LFF	6.53	6.49	6.37	6.24
	Difference	0.021	0.109	0.037	0.018

Notes. The small region is a box centered on the loop structure connecting regions 1^- and 3^+. The full volume is in the whole computation domain. All values for energy are reports in units of 10^{32} erg. Associated errors in the calculation of the LFF energy and the energy difference are on average ±0.01 (±0.03) and a maximum of ±0.03 (±0.05) at 11:11 UT for the small region (full volume).

of open flux continues to decrease and there is no flux left connecting regions 1^- to 4^+. The amount of flux connecting region 1^- to region 1^+ increases by an additional 9%. There are marginal changes in the flux connecting 1^- to 2^+ and 3^+.

Following from the investigation of the changing magnetic flux within the region and the significant changes in connectivity, an investigation was undertaken into the energy stored in the magnetic field. Table 3 shows the calculated magnetic energy for two volumes: one centered on the loop structure connecting regions 1^- and 3^+ (see boxed region outlined in Figure 6) and the other being the full computational volume. An estimate of the error in the energy calculations is provided by calculating the energy of the LFF field for $\alpha_{\min} - \Delta_\alpha$, where $\Delta_\alpha = 0.17$[1] and $\alpha_{\min}$ is the calculated α value of the loop observed. From this, it is clear that there is a significant buildup in energy within both volumes from 09:35 UT to 11:11 UT. At 12:47 UT, the difference in magnetic energy between the potential and LFF field has significantly decreased and is only marginally higher than that at 09:35 UT, while at 14:27 UT this difference in magnetic energy is lower than at 09:35 UT.

5. CONCLUSIONS

NOAA 10956 rotated onto the solar disk on 2007 May 15 and 19 the region produced a B9 class flare, starting at 12:34 UT, peaking at 13:02 UT, and ending at 13:19 UT. The flare location suggests that the source of the flare was the loop structure connecting regions 1^- to 2^+ in our analysis. According to the *SOHO*/LASCO CME Catalog,[2] the region had an associated CME which first appeared at 13:24 UT in the C2 field of view. In addition, a disappearing filament was observed erupting from the lower right section of the regions beginning at 12:31 UT (Long et al. 2008).

Our analysis has highlighted a number of physical changes within the magnetic structure of the active region around this time. These are as follows:

1. Magnetic flux cancellation and emergence.
2. Increase in the amount of α or twist along the observed loop.
3. Changes in the connectivity between sub-regions.
4. Significant changes in the magnetic energy stored in the region.

The increase in the amount of twist or α along the observer loop from 09:35 UT to 11:11 UT was accompanied by an increase in the magnetic flux within sub-region 1^+, a decrease in the magnetic flux within sub-regions 1^- and 2^+, and an increase in the amount of magnetic energy stored within the volume. The increase in magnetic energy can be explained by the increase in α used to calculate it. However, as α is obtained from a comparison to EUV observations this increase is taken as real. Following the increase in α at 11:11 UT, the amount of twist along the observed loop decreases to 09:35 UT levels by 14:27 UT. During this time period, the magnetic flux in sub-regions 1^+, 1^-, 2^+, and 3^+ increases by $(0.4–1.5) \times 10^{20}$ Mx and there is a 1.1×10^{20} Mx decrease in the magnetic flux in region 4^+. Additionally, the magnetic energy decreases to 09:35 UT levels over the same time period. Changes in the connectivity from region 1^- can be associated with the changes in α prior to

[1] The step size of α during the cost function analysis is $\Delta_\alpha = 0.17$.

[2] http://cdaw.gsfc.nasa.gov/CME_list/index.html

11:11 UT. However, by 12:47 UT the amount of flux connecting to region 1^- to regions 1^+ and 3^+ rose significantly.

From 09:35 UT to 11:11 UT, the difference in magnetic energies increased from 1.3×10^{30} to 6.1×10^{30} erg in the sub-volume centered on the observed loop and from 2.1×10^{30} to 10.9×10^{30} erg in the full computational domain. This result is particularly important as the energy calculation at 11:11 UT is significantly different from the potential case, as indicated by the error estimate. It should be noted that smaller error bounds may be possible provided that a more detailed analysis of the cost function (smaller Δ_α) is performed and that a clear minimum is the cost function exists. By 12:47 UT, this difference in magnetic energy in the system had dropped by a factor of 3 and by 14:27 UT had decreased below the difference at 09:35 UT. The buildup and subsequent decrease in magnetic energy in the system is correlated with the mechanisms thought to be responsible for the release of the B9 flare at 12:30 UT. The method is unable to calculate the free energy of the system due to the limitations of LFF methods (Seehafer 1978). However, the reported changes in the difference in magnetic energy between the potential and LFF fields provide an estimate for changes in the free energy contained in the region during this time.

The above investigation of magnetic properties of NOAA 10956 has shown that from 09:35 UT there was a significant amount of flux cancellation within the region, accompanied by an increase in the amount of twist and free energy along the observed loop. Following the onset of the flare at 12:34 UT, the amount of twist and magnetic energy in the loops decreased. This was accompanied by the decrease in open flux leaving region 1^- and increase in the magnetic flux in the region. It is suggested that the sudden decrease and subsequent increase in magnetic flux within the active region and the changes in twist and magnetic energy caused small changes in the observed connectivity between sub-regions, Table 2. The emergence of magnetic flux within the region and resulting increase in magnetic energy could have resulted in the region passing a critical threshold, past which it was in an unstable configuration. Under the theory of self-organized criticality, this would have resulted in a series of events returning the region to a stable configuration (Vlahos & Georgoulis 2004). Whether the mechanism responsible for passing this critical threshold is the unbalanced emergence of flux within the region or the resulting non-potentiality of the flux ropes remains unknown. The decrease in both α and magnetic energy and increase in connectivity of loop connecting region 1^- to region 3^+ suggest that the loop had room to expand and relax into the neighboring sub-region following the flare and eruption in the neighboring sub-region.

The method described in this paper allows for the detailed analysis of the amount of current or α in coronal loop structures, and with the added use of the twin perspectives of *STEREO* EUVI images, is an expansion of the methods developed by Wiegelmann et al. (2005) and Carcedo et al. (2003). These previous studies involved the use of cost functions as a mechanism for constraining the free parameters in extrapolations of the solar corona and were restricted to the investigation of one or two properties and singular instances in time. More advanced NLFF methods have been used to investigate the free magnetic energy of active regions (Régnier & Priest 2007; Schrijver et al. 2008) and in some instance its evolution (Thalmann & Wiegelmann 2008; Thalmann et al. 2008). However, these methods have been restricted by the limited time cadence of vector magnetogram data and provided little detail into the physical changes in the structure of active regions surrounding the buildup and release of magnetic energy. While the methods developed here are unable to accurately calculate the free energy of the active region, changes in the energy difference can be used as a proxy to changes in the free energy.

The method has been shown to detect changes in the amount of twist (and hence current) within coronal loop structures using the twin perspective of *STEREO*. Coupling the temporal analysis of the structure of NOAA 10956 with an investigation of the magnetic flux within each sub-region has provided great insight into the evolution and driving forces within the active region. Future work is needed improve the method and remove the need for user input. Expanding the method for the analysis of multiple loop structures in active regions would greatly increase the diagnostic power of the algorithm.

We are grateful to the referees for their helpful comments. P.A.C. is an IRCSET Government of Ireland Scholar funded under the Irish National Development Plan. The authors thank Dr. R. T. J. McAteer and Dr. D. S. Bloomfield for their helpful discussions and thoughts. The LFF method used in this study is an adaptation of the code originally developed by Dr. Thomas R. Metcalf.

REFERENCES

Alissandrakis, C. E. 1981, A&A, 100, 197
Aschwanden, M. J., Lee, J. K., Gary, G. A., Smith, M., & Inhester, B. 2008a, Sol. Phys., 248, 359
Aschwanden, M. J., Newmark, J. S., Delaboudinière, J., Neupert, W. M., Klimchuk, J. A., Gary, G. A., Portier-Fozzani, F., & Zucker, A. 1999, ApJ, 515, 842
Aschwanden, M. J., Wuelser, J., Nitta, N. V., Lemen, J. R., & Sandman, A. 2009, ApJ, 695, 12
Aschwanden, M. J., Wülser, J.-P., Nitta, N. V., & Lemen, J. R. 2008b, ApJ, 679, 827
Brosius, J. W., & White, S. M. 2006, ApJ, 641, L69
Burnette, A. B., Canfield, R. C., & Pevtsov, A. A. 2004, ApJ, 606, 565
Carcedo, L., Brown, D. S., Hood, A. W., Neukirch, T., & Wiegelmann, T. 2003, Sol. Phys., 218, 29
DeRosa, M. L., et al. 2009, ApJ, 696, 1780
Emslie, A. G., et al. 2004, J. Geophys. Res. (Space Phys.), 109, 10104
Gary, G. A. 1989, ApJS, 69, 323
Gary, G. A. 2001, Sol. Phys., 203, 71
Howard, R. A., Moses, J. D., & Socker, D. G. 2000, Proc. SPIE, 4139, 259
Leka, K. D., & Skumanich, A. 1999, Sol. Phys., 188, 3
Lim, E.-K., Jeong, H., Chae, J., & Moon, Y.-J. 2007, ApJ, 656, 1167
Longcope, D. W. 2001, Phys. Plasmas, 8, 5277
Longcope, D. W., Barnes, G., & Beveridge, C. 2009, ApJ, 693, 97
Longcope, D. W., & Beveridge, C. 2007, ApJ, 669, 621
Long, D. M., Gallagher, P. T., McAteer, R. T. J., & Bloomfield, D. S. 2008, ApJ, 680, L81
Metcalf, T. R., Jiao, L., McClymont, A. N., Canfield, R. C., & Uitenbroek, H. 1995, ApJ, 439, 474
Metcalf, T. R., Leka, K. D., & Mickey, D. L. 2005, ApJ, 623, L53
Metcalf, T. R., Mickey, D. L., Labonte, B. J., & Ryder, L. A. 2002, in Multi-Wavelength Observations of Coronal Structure and Dynamics, ed. P. C. H. Martens & D. Cauffman (New York: Elsevier), 249
Mikic, Z., Schnack, D. D., & van Hoven, G. 1990, ApJ, 361, 690
Pevtsov, A. A., Canfield, R. C., & Metcalf, T. R. 1994, ApJ, 425, L117
Pevtsov, A. A., Canfield, R. C., & Metcalf, T. R. 1995, ApJ, 440, L109
Phillips, K. J. H., Chifor, C., & Landi, E. 2005, ApJ, 626, 1110
Régnier, S., & Priest, E. R. 2007, ApJ, 669, L53
Scherrer, P. H., et al. 1995, Sol. Phys., 162, 129
Schrijver, C. J., et al. 2006, Sol. Phys., 235, 161
Schrijver, C. J., et al. 2008, ApJ, 675, 1637
Seehafer, N. 1978, Sol. Phys., 58, 215
Thalmann, J. K., & Wiegelmann, T. 2008, A&A, 484, 495
Thalmann, J. K., Wiegelmann, T., & Raouafi, N. 2008, A&A, 488, L71
Vlahos, L., & Georgoulis, M. K. 2004, ApJ, 603, L61
Wiegelmann, T., Inhester, B., Lagg, A., & Solanki, S. K. 2005, Sol. Phys., 228, 67